

Superconductor-insulator transition in an anisotropic two-dimensional electron gas assisted by one-dimensional Friedel oscillations: (Tl, Au)/Si(100)-c(2 × 2)

N. V. Denisov,¹ A. V. Matetskiy,^{1,*} A. N. Mihalyuk,^{1,2} S. V. Eremeev,^{3,4} S. Hasegawa,⁵ A. V. Zotov,^{1,2} and A. A. Saranin^{1,2}

¹*Institute of Automation and Control Processes, Far Eastern Branch of the RAS, Vladivostok 690041, Russian Federation*

²*Far Eastern Federal University, Vladivostok 690950, Russian Federation*

³*Institute of Strength Physics and Materials Science, Siberian Branch of the RAS, Tomsk 634055, Russian Federation*

⁴*Tomsk State University, Tomsk 634050, Russian Federation*

⁵*Department of Physics, University of Tokyo, Tokyo 113-0033, Japan*

 (Received 29 May 2019; revised manuscript received 25 September 2019; published 14 October 2019)

The recently found (Tl, Au)/Si(100)c(2 × 2) two-dimensional compound which possesses spin-split surface states with peculiar spin texture and strong band anisotropy was examined using low-temperature scanning tunneling microscopy and scanning tunneling spectroscopy observations and *in situ* four-probe transport measurements. Two types of the one-dimensional incommensurate Friedel oscillations were found to develop near the surface defects with the wavelengths corresponding to the nesting vectors of the (Tl, Au)/Si(100)c(2 × 2) Fermi surface. In transport measurements, samples show strong localization behavior when density of defects is sufficiently high. With low density of defects, the system demonstrates a metallic behavior with fingerprints of superconducting transition at estimated $T_c = 1.33$ K. Thus, the (Tl, Au)/Si(100)c(2 × 2) system hosts a combination of fascinating properties and effects, including one-dimensional Friedel oscillations, superconductivity, and a spin-split anisotropic Fermi surface, that opens an avenue for prospective investigations of the interplay of collective electronic phenomena in atomic layer material.

DOI: [10.1103/PhysRevB.100.155412](https://doi.org/10.1103/PhysRevB.100.155412)

I. INTRODUCTION

Systems with the reduced dimensionality constitute one of the most fascinating objects of the modern condensed-matter physics. The interest is driven not only by the possible difference of their atomic and electronic band structures from those of the bulk, reflected by the macroscopic properties, but also by the rich abundance of specific physical phenomena. From the viewpoint of the electronic transport, the metallic systems with reduced dimensionality do not look competitive due to the theoretical predictions of electron localization in them [1–3]. Impurities produce the barriers and act as strong scatterers. Moreover, the impurity potential induces a modulation of electron density with $2k_F$ periodicity known as the Friedel oscillations that also act as a scatterer [4–6]. In comparison with the three-dimensional case, Friedel oscillations in the low-dimensional systems are known to be more pronounced in their amplitude [7] and decay length [6,8], leading to a notable reduction of the electron density at the Fermi level [9].

Although Friedel oscillations are a product of electron-electron interaction, electron-phonon interactions also could lead to modulation of electron density via transition to a charge-density-wave (CDW) phase. In a simple one-dimensional (1D) model suggested by Peierls, the driven force of the CDW phase transition is an energy gain from the gap opening at certain Fermi vectors k_F , which provide a good Fermi-surface (FS) nesting (easily satisfied in the 1D case).

In addition to processes mentioned above which shatter the conductivity, some delocalization term can be gained from the spin-orbit coupling [10]. In general, however, the only way for the two-dimensional (2D) system to stay conductive at low temperatures is to become a superconductor [11,12]. Superconductivity is a collective phenomenon which relies on a number of electrons near the Fermi level and, thus, is bound tightly with other electron-density variation effects [13]. Typically, gapping due to the CDW and Friedel oscillations struggles the FS and, thus, can destroy conditions for superconductivity (SC) [14] and, generally, tuning the system to suppress CDWs is favorable for SC [15–22]. The same is true for charge-density suppression induced by disorder [23,24].

In the present paper, we have explored the low-temperature behavior of the recently found (Tl, Au)/Si(100)c(2 × 2) reconstructed surface [25]. The system is of interest because it was proved to possess a set of very specific features. It is purely two dimensional and consists of only two (Tl and Au) monolayers ($1 \text{ ML} = 6.8 \times 10^{14} \text{ cm}^{-2}$). It has metallic surface states that is uncommon for the metal-induced reconstructions on the Si(100) surface due to its loose packing. Its Fermi surface is strongly anisotropic and, thus, could provide good “nesting” at selected Fermi wave-vectors k_F . Its surface states are spin split due to the Rashba effect and display peculiar spin texture due to the C_{2v} symmetry of the system. In the present paper, we have found that this system demonstrates a set of various effects, including strongly anisotropic electron scattering leading to the 1D Friedel oscillations, transition either into superconducting or insulating states depending on the defect density and Anderson

*mateckij@iacp.dvo.ru

localization. Their interplay has been investigated using scanning tunneling microscopy/scanning tunneling spectroscopy (STM/STS) observations and *in situ* transport and magneto-transport measurements at low temperatures.

II. EXPERIMENTAL AND CALCULATION DETAILS

The experiments were performed in the UNISOKU USM 1500 LT STM system, equipped with the superconducting magnet and four-point-probe (4PP) technique, which provides the lowest temperature of 1.7 K and magnetic field up to 8 T perpendicular to the sample. The base pressure was 1×10^{-10} Torr. Atomically clean Si(100) 2×1 surfaces were prepared *in situ* by flashing to 1250 °C for 25 s after the samples were first annealed at 830 °C for 1 h. Thallium was deposited from the Ta tube and gold from the Au-wrapped W filament. In order to form the (Tl, Au)/Si(100) $c(2 \times 2)$ compound, the two-step procedure was used [25]. At the first step, thallium was adsorbed onto the Si(100) 2×1 surface held at room temperature (RT) to form the Tl/Si(100) 2×1 phase which is known to incorporate 1.0 ML of Tl atoms arranged in the structure described by the pedestal + valley-bridge model [26]. At the second step, 1.0 ML of Au was deposited onto the Tl/Si(100) 2×1 phase at RT that leads to the developing (Tl, Au)/Si(100) $c(2 \times 2)$ compound. Note that the compound periodicity can also be described by the $(\sqrt{2} \times \sqrt{2})$ - $R45^\circ$ primitive unit mesh.

Topographical STM images were acquired in a constant-current mode with a mechanically cut PtIr tip after annealing in vacuum. Differential conductance (dI/dV) STM images were acquired using a lock-in technique with a modulation amplitude of 20 mV and a frequency of 1.983 kHz. The 4PP head with a linear probe geometry mount on the STM stage instead of the tip holder was used for the *in situ* transport measurements. Gold wires of 0.1 mm in diameter equally spaced by 0.2 mm were used for the probes. Ohmic linear $I(V)$ behavior of the contacts was checked at the beginning and the end of each measurement.

Our calculations were based on density functional theory (DFT) as implemented in the Vienna *ab initio* simulation package VASP [27,28] using a plane-wave basis set. The projector-augmented-wave (PAW) approach [29] was used to describe the electron-ion interaction. The local density approximation (LDA) [30] to the exchange-correlation functional was employed. To improve the band gap of the silicon substrate for band-structure calculations, we used the LDA-1/2 self-energy correction method [31,32] for the correction of the Si PAW. To simulate the Tl-Au reconstruction on Si(100), we used a slab consisting of 40 single layers (SLs) of silicon at the LDA-optimized bulk Si lattice constant. Hydrogen atoms were used to passivate the Si dangling bonds at the bottom of the slab. The atomic positions of adsorbed atoms and atoms of Si layers within the six SLs of the slab were optimized. Silicon atoms of the deeper layers were kept fixed at the bulk crystalline positions. The plane-wave cutoff energy was 250 eV. The band structure of such a slab completely reproduces the surface spectrum obtained in Ref. [25] for (Tl, Au)/Si(100) $c(2 \times 2)$ with 60 Si layers. For the calculation of the electron-density maps, we used a dense k -point mesh (with a distance between neighboring k points

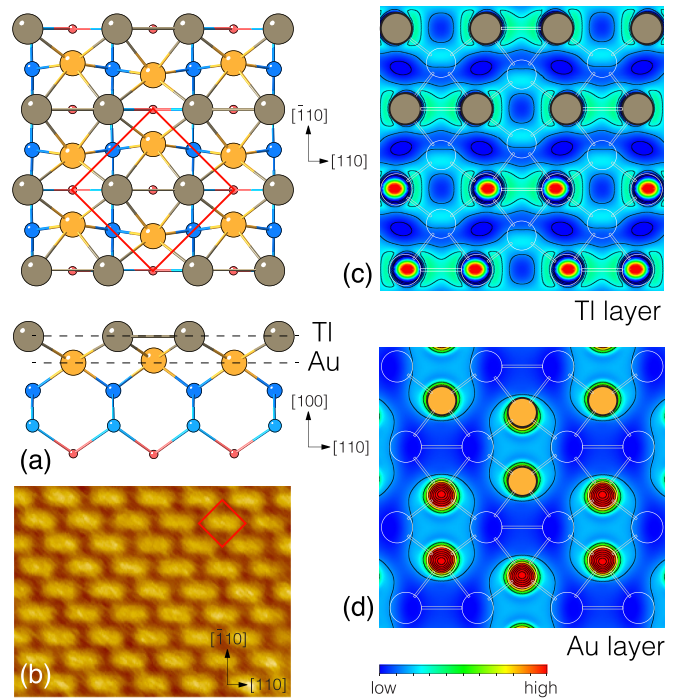


FIG. 1. (a) Ball-and-stick model and (b) high-resolution filled-state (-1.5 -V) STM image of the (Tl, Au)/Si(100) $c(2 \times 2)$ surface. Thallium atoms are shown by gray balls, gold atoms by yellow balls, and Si atoms by small blue and pink balls depending on the layer. The primitive $(\sqrt{2} \times \sqrt{2})$ - $R45^\circ$ cell is outlined by a red square. Calculated electron-density maps for (c) Tl and (d) Au layers within the (Tl, Au)/Si(100) $c(2 \times 2)$ compound. In the upper parts of the figures (c) and (d), Tl and Au atoms, shown by gray and yellow circles, respectively, are superposed on the maps.

of about 0.02 \AA^{-1} and more than 500 points in total) in the areas of the Fermi contours. The integration range was from the Fermi level down to -50 meV with Gaussian smearing of 10 meV.

III. RESULTS AND DISCUSSION

A. Atomic structure

As determined in Ref. [25], the atomic structure of the (Tl, Au)/Si(100) $c(2 \times 2)$ compound can be visualized as a double-layer atomic sandwich where a single atomic layer of Tl resides above a single atomic layer of Au lying on the bulk-like-truncated Si(100) surface [25] [Fig. 1(a)]. The compound has an anisotropic structure with a C_{2v} symmetry. In particular, the Tl atoms in the top atomic layer are dimerized having the nearest-neighbor Tl-Tl distance of 3.44 Å which is close to the Tl-Tl bulk value of 3.40 Å. In addition, in the electron-density map [Fig. 1(c)], one can even note a certain motif for the quasi-one-dimensional behavior as indicated by occurrence of the conduction channels along the Tl-Tl dimer direction. In contrast, the Au layer exhibits less extent of anisotropy; in particular, there is only a weak indication on the dimerization: although the nearest Au-Au distance of 3.30 Å is less than that for the Tl-Tl pairs, but it far exceeds the bulk Au-Au value of 2.88 Å. Moreover, any distinct quasi-one-dimensional

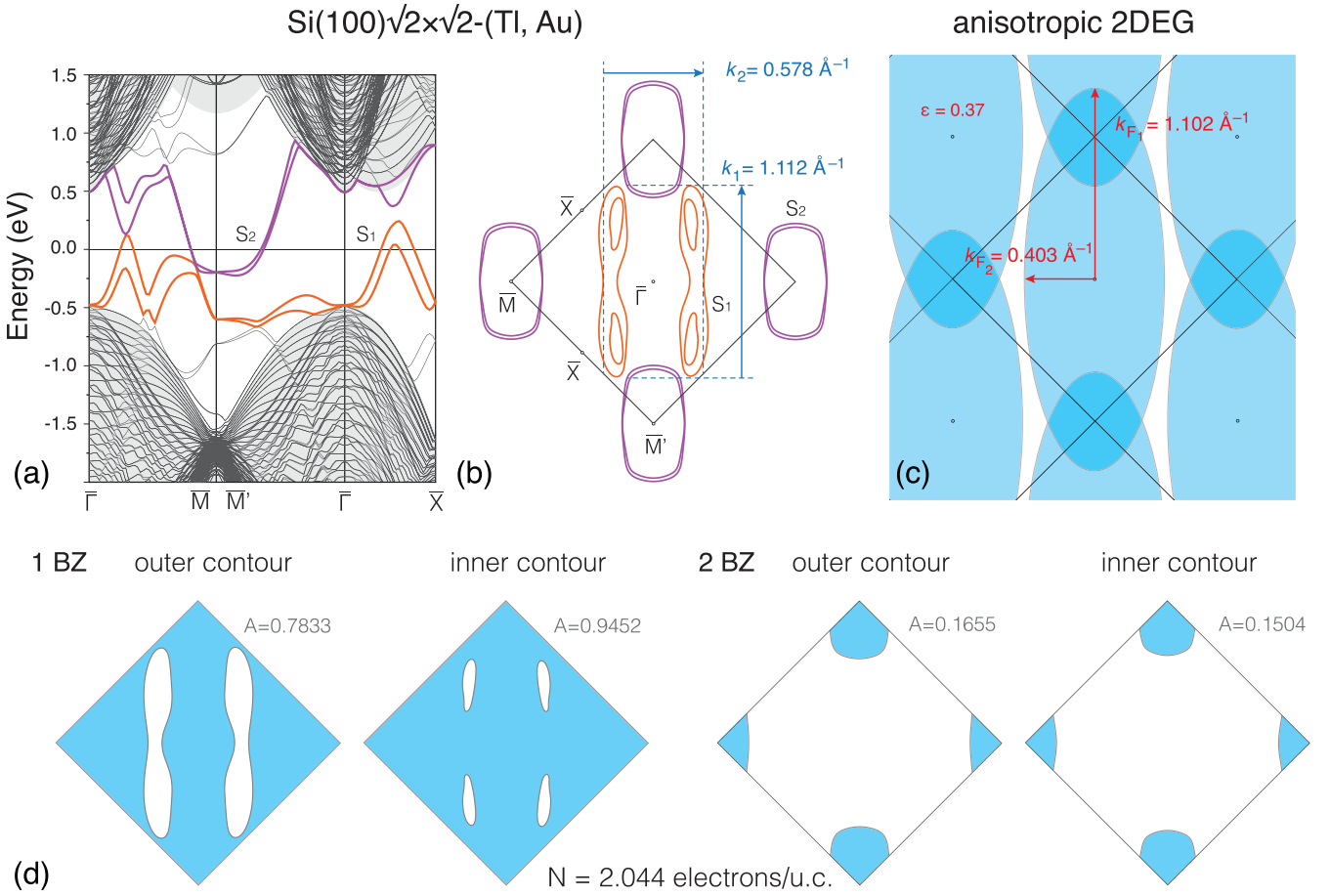


FIG. 2. (a) Electronic band dispersions and (b) Fermi-contour map of the (TI, Au)/Si(100) $c(2 \times 2)$ compound. The S_1 and S_2 surface-state bands are indicated by red and blue colors, respectively. The nesting vectors k_1 and k_2 for the “short”-period and “long”-period CDWs, respectively, are indicated in (b). (c) Harrison’s construction of the Fermi surfaces for the anisotropic 2D electron gas superposed with an extended $\sqrt{2} \times \sqrt{2}$ surface Brillouin zones (SBZs). (d) Fermi surfaces of the real (TI, Au)/Si(100) $c(2 \times 2)$ in the first and second SBZs for inner and outer contours with indicated electron filling of the corresponding zones.

conduction channels are lacking in the electron-density map of the Au layer [Fig. 1(d)].

B. Electronic properties

Figure 2 illustrates the main peculiarities of the electron band structure of the (TI, Au)/Si(100) $c(2 \times 2)$ system. In particular, Fig. 2(a) shows electron dispersion curves as determined using angle-resolved photoemission spectroscopy (ARPES) measurements and DFT calculations in Ref. [25]. One can see that there are two metallic surface-state bands crossing the Fermi level, the holelike S_1 band (shown in red) and the electronlike S_2 band (shown in violet). Both bands are spin split. Detailed description of their spin texture is given elsewhere [25]. In the Fermi-contour map [Fig. 2(b)], the S_2 band forms two concentric contours having the shape of a rounded rectangle around the \bar{M} (\bar{M}') points. The S_1 band yields a pair of bean podlike features, each containing the outer warped-elliptical-shaped and two inner bean-shaped contours. The origin of the bands having these shapes can be qualitatively understood constructing the Fermi surfaces for the free electrons according to a procedure credited to

Harrison. In the case of the *isotropic* degenerated 2D free-electron gas, the Fermi vector is given by

$$k_F = \sqrt{2\pi n_e}, \quad (1)$$

where n_e is the 2D electron density and the Fermi surface is a circle with a radius of k_F . However, the (TI, Au)/Si(100) $c(2 \times 2)$ surface is *anisotropic*, and one can see that superposing of the circular Fermi surface onto the square lattice could hardly reproduce the shape of the real Fermi contours. A simple but reasonable guess that the anisotropic electronic band structure is simulated better by the Fermi surface having a shape of an ellipse rather than a circle provides a hint for understanding the origin of the (TI, Au)/Si(100) $c(2 \times 2)$ Fermi contours. Figure 2(c) shows Harrison’s construction for the elliptic Fermi surface. Indeed, one can note a clear principal resemblance between simulated Fermi surface and that of the real (TI, Au)/Si(100) $c(2 \times 2)$ surface [Figs. 2(c) and 2(d)]. The only essential difference is due to the lattice potential effect which changes the simulated open quasi-one-dimensional Fermi surface to the real closed Fermi surface with bean podlike hole pockets. In the framework of this scheme, evaluation of the electron filling

of the first and second SBZs of (Tl, Au)/Si(100) $c(2 \times 2)$ [Fig. 2(d)] yields 2.044 electrons per $\sqrt{2} \times \sqrt{2}$ unit cell, i.e., $6.9 \times 10^{14} \text{ cm}^{-2}$. For the isotropic circular Fermi surface, this would correspond to $k_F = 0.660 \text{ \AA}^{-1}$. The best simulation of the anisotropic case is achieved with the Fermi ellipse having a semiminor axis $k_{F_1} = 0.403 \text{ \AA}^{-1}$, a semimajor axis $k_{F_2} = 1.102 \text{ \AA}^{-1}$, and an eccentricity $\varepsilon = 0.37$ as shown in Fig. 2(c), which ensures the same electron filling of the SBZs as in reality. Thus, one can conclude that the electronic system of the (Tl, Au)/Si(100) $c(2 \times 2)$ surface is strongly anisotropic representing a transient case between two-dimensional and quasi-one-dimensional systems.

C. Fast Fourier transform and STS analysis

Figure 3 shows [(a) and (c)] topographical and [(b) and (d)] differential-conductance (dI/dV) STM images of the (Tl, Au)/Si(100) $c(2 \times 2)$ surface of large and small scales, respectively. One can note that the original $c(2 \times 2)$ pattern is distorted by the two wavy modulations having different wavelengths and propagating in the orthogonal directions. They are pronounced near the defects and damp away from them and can be associated either with the QPI, termed also Friedel oscillations [33,34], or with the CDWs. We are reminded that the most essential difference between QPI and CDW resides in the dependence of their periods on energy, hence, on the bias voltage at which the STM image was acquired. Whereas, in the QPI, the period of modulations varies with bias following the electron band dispersion, in the case of the CDWs, the period is bias independent. Thus, in order to elucidate the nature of the observed modulations, we conducted FFT analysis of the topographical and dI/dV STM images at various sample biases.

Since the (Tl, Au)/Si(100) $c(2 \times 2)$ system has C_{2v} symmetry, the diagonal directions (i.e., the basic directions for Si(100), $[\bar{1}10]$, and $[110]$) are not equivalent. Thus, electronic band dispersions are different along the $\bar{\Gamma M}'$ and $\bar{\Gamma M}$. In the current STM observation, we conducted FFT analysis within a single particular terrace, that is in contrast to the space-integrated ARPES measurements. Thus, the data along the $\bar{\Gamma M}'$ and $\bar{\Gamma M}$ directions can be evaluated separately. Note that we ascribe the $\bar{\Gamma M}'$ direction to the one perpendicular to the Tl-dimer bond and the $\bar{\Gamma M}$ direction to that parallel to the Tl-dimer bond. As a result, in the FFT analysis, we studied dispersion of the short-period modulations in the $\bar{\Gamma M}'$ direction and the long-period modulations in the $\bar{\Gamma M}$ direction.

Figures 3(g)–3(j) present the results of the FFT analysis in the form of the FFT maps, i.e., bias-dependent profiles of the FFT-processed topographical [Figs. 3(g) and 3(i)] and dI/dV [Figs. 3(h) and 3(j)] STM images in the $\bar{\Gamma M}'$ [Figs. 3(g) and 3(h)] and $\bar{\Gamma M}$ [Figs. 3(i) and 3(j)] directions. The bias-independent 1×1 spot appears in all FFT maps at 1.63 \AA^{-1} . It corresponds to the doubled $\bar{\Gamma}-\bar{X}$ distance of the 1×1 SBZ and to the doubled $\bar{\Gamma}-\bar{M}$ distance of the $\sqrt{2} \times \sqrt{2}$ SBZ [see Figs. 3(d) and 3(f)].

Let us consider first the FFT maps obtained from dI/dV STM images [Figs. 3(h) and 3(j)]. Along the $\bar{\Gamma M}'$ direction,

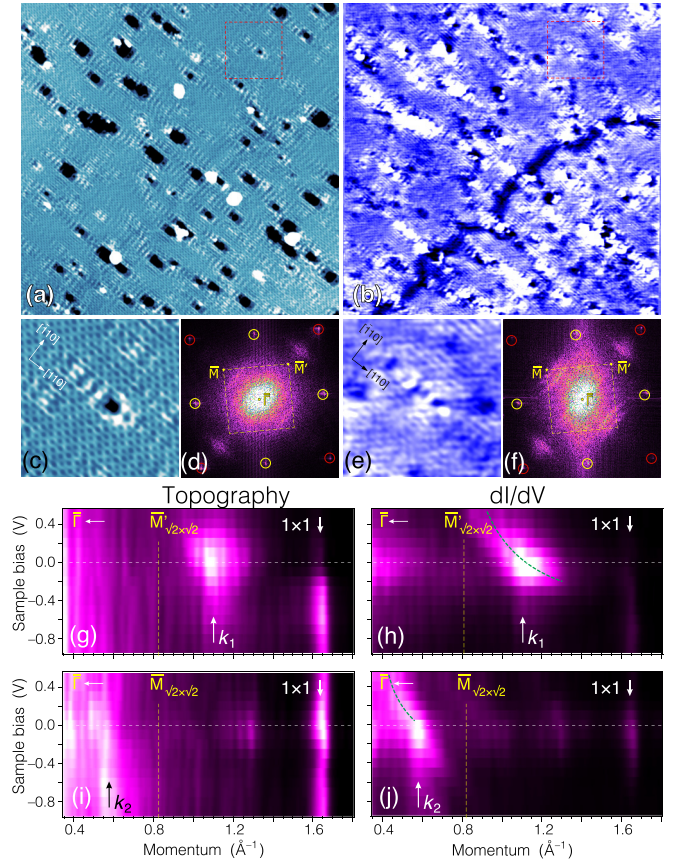


FIG. 3. Fast Fourier transform (FFT) analysis of the (Tl, Au)/Si(100) $c(2 \times 2)$ surface. Typical $55 \times 55\text{-nm}^2$ filled-state (-0.5-V) STM images of (a) topography and (b) conductance (dI/dV) obtained from a single Si(100) terrace at 6 K. The red dashed squares in (a) and (b) outline the $10 \times 10 \text{ nm}^2$ areas shown at a greater magnification in (c) and (e), respectively. (d) and (f) FFT images obtained from (a) and (b), respectively. The red and yellow circles mark the 1×1 and $\sqrt{2} \times \sqrt{2}$ spots, respectively. The $\sqrt{2} \times \sqrt{2}$ SBZ is outlined by yellow dashed lines with high-symmetry points $\bar{\Gamma}$, \bar{M}' , and \bar{M} , indicated. Experimental FFT maps extracted from (g) and (i) topographical and (h) and (j) dI/dV STM images along the (g) and (h) $\bar{\Gamma M}'$ and (i) and (j) $\bar{\Gamma M}$ directions. The green dotted lines in (h) and (j) mark the dispersive quasiparticle interference (QPI) bands associated with scattering on the surface states. The 1×1 spot is indicated. The nondispersive branch with wave-vector $k_1 = 1.11 \text{ \AA}^{-1}$ associated with the short-period CDWs and that with wave-vector $k_2 = 0.58 \text{ \AA}^{-1}$ associated with the long-period CDWs and indicated by arrows in (g) and (h) and (i) and (j), respectively.

the QPI phenomena could occur due to scattering of the S_2 band electrons. This band forms electron pockets around the M points with minima at -0.3 eV [Figs. 2(a) and 2(b)]. Indeed, this feature can be observed in the corresponding FFT map [marked by the green dotted line in Fig. 3(h)]. In addition, one can note a bias-independent feature at negative biases at $k_1 = 1.11 \text{ \AA}^{-1}$ having a wavelength of $\lambda_1 = 2\pi/k_1 = 5.65 \text{ \AA}$ and aligned along the $[\bar{1}10]$ direction (i.e., perpendicular to the Tl-dimer-bond direction). In the FFT map for the $\bar{\Gamma M}$ direction [Fig. 3(j)], one can see the dispersive QPI feature

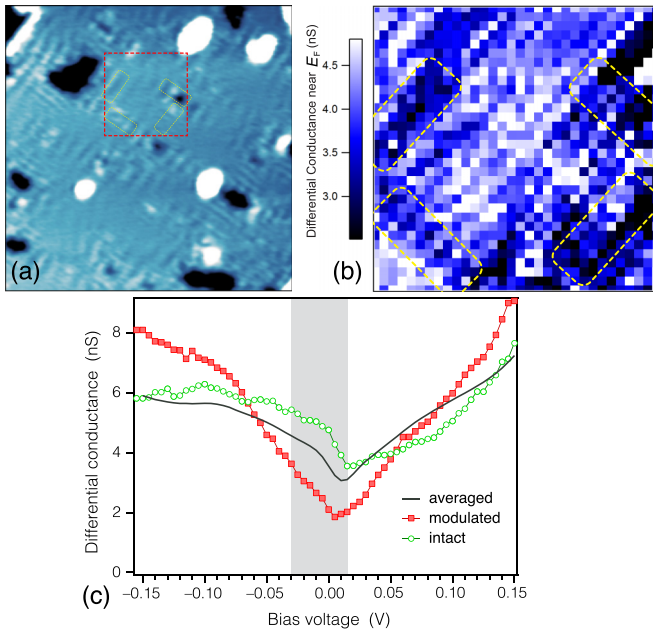


FIG. 4. STS analysis of the (Ti, Au)/Si(100) $c(2 \times 2)$ surface. (a) Topographical STM image ($25 \times 25 \text{ nm}^2$) where the intact undisturbed $c(2 \times 2)$ area surrounded by the areas with modulations is outlined by a purple square. (b) STS dI/dV map recorded at a bias close to zero [averaged over the hatched bias range in (c)] within a $(7 \times 7)\text{-nm}^2$ area outlined by a red dashed square in (a). Modulated regions are outlined by yellow dashed rounded rectangles. (c) STS dI/dV spectra taken from the intact area (green circles and line), outlined modulated areas (red circles and line), and averaged spectrum (black line).

at positive voltages [marked by the green dotted line in Fig. 3(j)], that could be associated with the S_1 band. Besides, one can see the bias-independent feature at $k_2 = 0.58 \text{ \AA}^{-1}$ that is especially pronounced at negative voltages and has a wavelength $\lambda_2 = 2\pi/k_2 = 10.87 \text{ \AA}$ aligned along the [110] direction (i.e., along the Ti-dimer-bond direction). Note that both waves are incommensurate with respect to the underlying Si(100) substrate as the short wavelength $\lambda_1 = 1.47a_0$ and the long wavelength $\lambda_2 = 2.83a_0$, where $a_0 = 3.84 \text{ \AA}$ is the lattice constant of the Si(100) surface. In the FFT maps extracted from the topographical STM images [Figs. 3(g) and 3(i)], one can see the presence of the same features as in the dI/dV FFT maps.

We performed also the space-resolved STS measurements in the area where modulated and relatively intact surface regions could be found (Fig. 4). In the modulated regions, the recorded STS shows a lower density of states (DOS) near a zero bias as compared to that at the intact (Ti, Au)/Si(100) $c(2 \times 2)$ surface [Fig. 4(c)]. Moreover, this DOS-depleted region reproduces the position and 1D character [Fig. 4(b)] of the characteristic modulations in the topographical image. According to the STS data in Fig. 4(c), the size of the partial gap could be as large as $\sim 100 \text{ meV}$. Indeed, we observed wavy patterns at 78 K, and similar modulations were seen at the previous RT-STM measurements [25]. However, it should be noted that the gap structure is not

clearly visible in the dI/dV curves, and they do not reach zero at zero bias voltage.

Let us consider now the origin of the wavy patterns observed on the surface. On one hand, they exhibit a number of features that can be interpreted as fingerprints of CDWs. First, they display bias-independent features in the FFT maps, including those extracted from the topographical STM images. Second, it is known that if the CDW wavelength is incommensurate with the lattice period the CDW is pinned by lattice defects to minimize CDW energy by adjusting its position so as to place a crest or trough at the defect [35]. This is consistent with patterns seen in the STM images from the (Ti, Au)/Si(100) $c(2 \times 2)$ surface. Third, in the case of CDWs having a Peierls-instability origin, there should be corresponding nesting vectors for the Fermi surface in the given directions. The waves in the $\overline{\Gamma M'}$ direction have the short wavelength of $\lambda_1 = 5.65 \text{ \AA}$ and the nesting vector $k_1 = 2\pi/\lambda_1 = 1.11 \text{ \AA}^{-1}$ which bounds the electron pockets around the M' points. The waves in the $\overline{\Gamma M}$ direction have the long wavelength of $\lambda_2 = 10.9 \text{ \AA}$ and the nesting vector $k_2 = 2\pi/\lambda_2 = 0.58 \text{ \AA}^{-1}$ which bounds contours of elongated bean-shaped hole pockets located in between the $\overline{\Gamma}$ and the \overline{M} points. The nesting vectors k_1 and k_2 are shown in the Fermi-contour map in Fig. 2(b). Fourth, the CDW formation is accompanied by the gap opening that should be seen in the STS measurements. Indeed, in the modulated regions, the recorded STS spectra show, at least, a lower DOS near a zero bias as compared to that at the intact surface [Fig. 4(c)]. However, these arguments do not seem to be solid enough for the conclusive proof of the CDW scenario.

There is a set of other findings that sound against the charge-density wave origin of the observed wavy patterns and favor the QPI scenario. First, in the CDW case, the bias-independent features in the FFT maps would be observed in the whole energy range of the surface-state bands but not only in the limited energy regions as in Figs. 3(g)–3(j). Second, the large gap seen in the STS measurements in Fig. 4(c) implies that all observations are conducted well below the possible CDW transition. Hence, the CDW phase should cover the whole surface even a case of the incommensurate CDWs [36–38]. On the present (Ti, Au)/Si(100) $c(2 \times 2)$ surface, the wavy patterns are seen only around the defects and fade out away from them. Such behavior is more typical for the Friedel oscillations [37]. Third, occurrence of the nesting vectors might be associated not only with the CDWs, but also with the QPI in the highly anisotropic media, causing occurrence of the one-dimensional Friedel oscillations. Fourth, gap formation is known to assist not only CDW formation, but also it takes place during the formation of the Friedel oscillations [39]. Fifth, the most important item is that CDW involves changing of atomic positions that should show up by appearance of specific reflections in the low-energy electron microscopy or reflection high-energy electron diffraction patterns. In the present paper, we did not detect such features. In conclusion, the whole data set implies that the appearance of the wavy patterns at the (Ti, Au)/Si(100) $c(2 \times 2)$ surface is not due to the true CDW transition, but rather there is a strong anisotropic scattering induced by defects which leads to developing of the 1D Friedel oscillations in the two orthogonal directions.

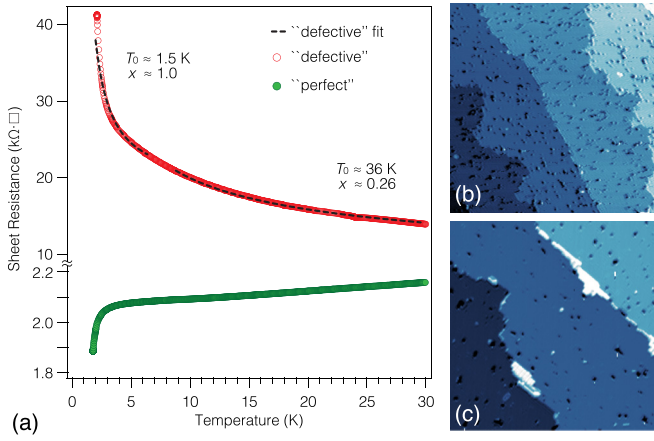


FIG. 5. (a) Temperature dependence of the sheet resistance of “defective” (Tl, Au)/Si(100) $c(2 \times 2)$ sample with high density of defects (open red circles) and “perfect” surface with minor defects (green circles). Note that the resistance scales for the two dependencies are different. Filled-state (-0.6 -V) (100×100)-nm² STM images of the (b) defective and (c) perfect (Tl, Au)/Si(100) $c(2 \times 2)$ surfaces.

D. Transport properties

The Si(100) surface is known to host several types of defects, such as missing dimers and dissociatively adsorbed water molecules, so-called C-defects [40,41]. Using the appropriate heat-treatment procedure, one can reduce concentration of these defects. However, the extent of success depends on vacuum conditions and sample holder/heater design. The defects of the initial Si(100) surface are typically inherited by the metal-induced reconstructions formed on this surface. In the case of the compound reconstruction, additional defects can also develop due to the deviations from the compound stoichiometry.

The transport properties of the (Tl, Au)/Si(100) $c(2 \times 2)$ have been found to depend crucially on the structural quality of the prepared surface as illustrated in Fig. 5. In the case of the highly ordered surface with a minor concentration of defects (to be called herewith the perfect surface), the sample shows a metallic behavior with a trend for transition into a superconducting state as indicated by a steep decrease in resistance when the temperature approaches the low limit of ~ 1.7 K accessible in the present transport measurements. The normal-phase resistance (e.g., measured at 10 K) equals ~ 2.1 kΩ. When concentration of defects is relatively high [as at the defective surface shown in Fig. 5(a)], sample resistance amounts to ~ 20 kΩ at 10 K which is very close to the resistance quantum ($h/e^2 = 25.813$ kΩ) and rapidly grows with decreasing temperature revealing the insulating behavior.

Using the Drude formula for the conductivity,

$$\sigma_0 = \frac{n_e e^2 \tau_0}{m}, \quad (2)$$

where e is the electron charge and m is the electron mass, we can estimate elastic relaxation time τ_0 , which appears to be 2.6 and 0.26 fs for the perfect and defective surfaces, respectively. As follows from the slope of the dispersions in the vicinity of the Fermi level in the experimental ARPES

spectra and calculated band structure, the Fermi velocity v_F for the S_1 and S_2 bands is essentially the same and equals 0.5×10^8 cm/s. Then, we can estimate the elastic relaxation length $l_0 = v_F \tau_0$, which appears to be 13.7 and 1.4 Å for the perfect and defective surfaces, respectively.

According to the Ioffe-Regel criterion [42], films having $k_F l_0 \gg 1$ are metallic, whereas films having $k_F l_0 \ll 1$ are insulating. (It is argued that a more proper comparison would be that with π rather than with 1 [43].) The Fermi surface of the (Tl, Au)/Si(100) $c(2 \times 2)$ is anisotropic, and k_F is different for the two orthogonal directions. For estimation, we can take semiminor axis k_{F_1} and semimajor axis k_{F_2} of the model elliptical Fermi surface shown in Fig. 2(c). In the case of the perfect surface, this leads to $k_{F_1} l_0 = 5.5$ and $k_{F_2} l_0 = 15.1$. Thus, the Ioffe-Regel criterion for the metallic conduction is clearly satisfied for one direction, whereas its fulfillment for the other direction is less evident. For the defective surface, the criterion is not satisfied for any direction in agreement with the results of the transport measurements which reveal its insulating behavior. The transport measurements on the surfaces where the defects were basically associated with the Tl deficit showed that metal-insulator transition took place when the sample resistance was ~ 6 kΩ, hence, at $k_{F_2} l_0 \sim 5$ (see the Supplemental Material 1 [44]).

At low temperatures, the elastic relaxation length l_0 (i.e., the mean distance an electron has traveled since the last collision) is controlled mainly by electron scattering at defects and is expected to be on the order of the mean distance between defects. However, comparison of l_0 derived above from evaluation of the results of transport measurements and the electron band structure with the mean distance between defects l_d seen in the STM images (evaluated as $l_d = n_d^{-1/2}$, where n_d is areal density of defects) reveals a great inconsistency. For the perfect surface, $l_0 = 13.7$ and $l_d = 98$ Å. For the defective surface, these values are 1.4 and 42 Å, respectively. One can see that the elastic relaxation length appears to be much shorter than the distance between defects. This result indicates that electrons are scattered not at the defects themselves but rather at the perturbations of the local electron density caused by formation of the Friedel oscillations around the defects. However, Friedel oscillations can only facilitate the transition into the insulating state through decreasing of the conductance in the modulated areas as seen in Fig. 4(c). The density of states around the Fermi level still remains, and, thus, Friedel oscillations solely are unable to cause transition into the insulating state, and Anderson localization seems to be the most natural explanation for this transition. In the insulating state in the 2D case, the temperature dependence of the resistance is considered to be of a variable-range hopping type and can be described by the universal expression of $\rho = \rho_0 \exp[(T_0/T)^x]$ with an exponent $x = (m+1)/(m+3)$, where m is an exponent of the density of states dependence $|E - E_F|^m$ near the Fermi energy [45,46]. With lowering the temperature, the Mott mechanism [47] with an exponent $x = 0.33$, which corresponds to the constant density of states, usually changes to the Efros-Shklovskii type [48] with $x = 0.5$, which corresponds to the parabolic gap. However, in some materials at low temperatures, a much stronger temperature dependence is observed with an exponent x larger than 0.5 [49]. Fitting of the temperature dependence of the resistance

for the defective sample [black dashed curves in Fig. 5(a)] yields the exponent values of $x \approx 1.0$ and $T_0 \approx 1.5$ K and $x \approx 0.26$ and $T_0 \approx 36$ K for low- and high-temperature ranges, respectively.

Let us consider now the conductivity of the perfect (Tl, Au)/Si(100)c(2 × 2) surface at temperatures close to the superconducting transition. Since the critical temperature T_c is lower than the limit accessible in our experimental system, the zero resistance state is not achieved. However, it is clearly seen that the resistance starts to decrease above the critical temperature. This is due to the fluctuation corrections to conductivity which play essential role in the low-dimensional systems. The most essential corrections include the Aslamazov-Larkin (AL) contribution σ_{AL} caused by the addition to the conductivity from fluctuating Cooper pairs and the Maki-Thompson (MT) contribution σ_{MT} corresponding to coherent scattering of electrons constituting a fluctuating Cooper pair by impurities.

The AL correction [50–52] is expressed as

$$\sigma_{AL}^{1D} = \frac{e^2 \xi(0)}{16 \hbar L \epsilon^{3/2}} \quad \text{for the 1D case,} \quad (3)$$

$$\sigma_{AL}^{2D} = \frac{e^2}{16 \hbar \epsilon} \quad \text{for the 2D case,} \quad (4)$$

where $\epsilon = \ln(T/T_c)$.

The AL correction for the 2D case contains only T_c as a single fitting parameter. The AL correction for the 1D case contains also the Ginzburg-Landau coherence length $\xi(0)$ and conduction channel length L .

The MT contribution is given by [52–54]

$$\sigma_{MT} = \frac{e^2}{8 \hbar \epsilon} \frac{1}{\epsilon - \delta} \ln \frac{\epsilon}{\delta}, \quad (5)$$

where δ is a pair-breaking parameter.

Figure 6 shows the temperature dependencies of the perfect (Tl, Au)/Si(100)c(2 × 2) sample resistance at the low temperatures close to superconducting transition measured without an applied magnetic field (blue circles) and with an applied magnetic field of 0.2, 0.5, and 1.0 T (green, yellow, and red circles, respectively). One can see that a system displays a clear field-induced superconductor-insulator transition. Unfortunately, determination of any quantitative characteristics, such as the Ginzburg-Landau coherence length or Berezinskii-Kosterlitz-Thouless transition temperature from the resistance measurements with the magnetic field is hampered by the inability to access the critical temperature with our experimental system. Therefore, we limit our consideration by the results of transport measurements at zero magnetic field.

The zero-field dependence was fitted using the AL correction with $T_c = 1.33$ K (for comparison, the bulk TlAu compound has $T_c = 1.92$ K [55]) for the 2D and 1D cases shown by dashed violet and solid blue lines, respectively. One can see that the best fit is achieved with the AL correction for the 1D case where the coincidence of the calculated curve and experimental data is almost ideal. In particular, this means that the MT contribution is negligible compared to the 1D AL correction. Note that attempts to improve the fit with the 2D

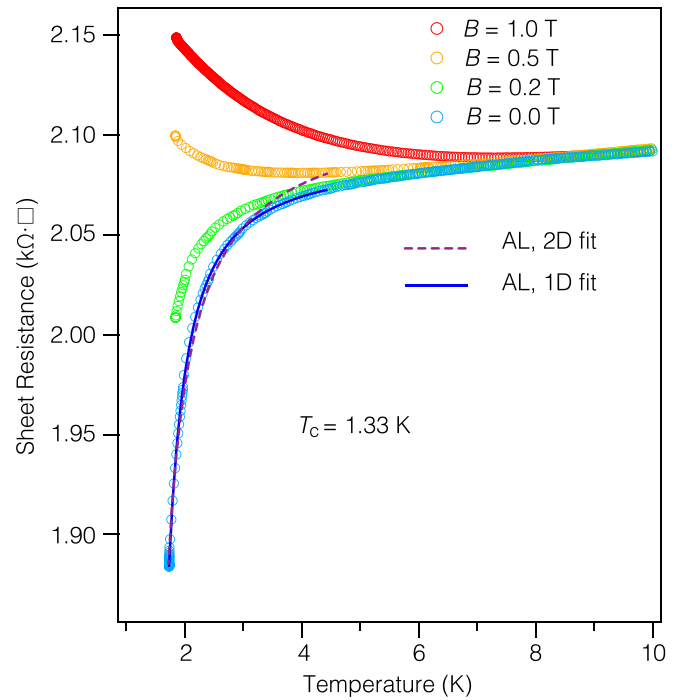


FIG. 6. Change in the sheet resistance of the perfect (Tl, Au)/Si(100)c(2 × 2) sample with temperature under different magnetic fields (0.0, 0.2, 0.5, and 1.0 T). The dashed violet and solid blue lines are the results of the least-squares fits to the Almazov-Larkin correction with $T_c = 1.33$ K for the 2D and 1D cases, respectively.

AL correction by adding any MT correction have no success (see Supplemental Material 2 [44]).

The negligible Maki-Thompson contribution can be formally attributed to a large pair-breaking parameter. The large magnitude of the pair-breaking interaction is thought to be associated with a large anisotropy of the superconducting order parameter and d -wave pairing symmetry [52,56–58]. Both characteristics are believed to be the peculiar features of the (Tl, Au)/Si(100)c(2 × 2) system. Indeed, the system is highly anisotropic, almost quasioverdimensional in structural, electronic, and transport properties, and Au d states have been proved to produce a noticeable contribution to the S_1 and S_2 surface-state bands in the vicinity of the Fermi level [25].

IV. CONCLUSION

In conclusion, we studied the (Tl, Au)/Si(100)c(2 × 2) reconstructed surface which consists of thallium and gold monoatomic layers, residing one atop another on the Si(100) surface, and possess properties of a highly anisotropic 2D electron gas. We found that due to a strong anisotropic scattering induced by defects the 1D Friedel oscillations develop at the surface in the two orthogonal directions. Depending on the defect density, the system at low temperatures undergoes transition either into superconducting or into insulating states. In the defective samples, an occurrence of the Friedel oscillations facilitates the transition into an insulator state which follows the Anderson localization scenario. The perfect samples

clearly show fingerprints of the transition into a quasi-one-dimensional superconductor at the estimated critical temperature $T_c = 1.33$ K. Thus, the (TI, Au)/Si(100) $c(2 \times 2)$ system hosts a combination of fascinating properties and effects, including one-dimensional Friedel oscillations, superconductivity, and a spin-split anisotropic Fermi surface, that opens an avenue for prospective investigations of the interplay of collective electronic phenomena in atomic layer material.

ACKNOWLEDGMENTS

The work was supported by the RSF Grant No. 19-12-00101. The part of the work devoted to low-temperature transport measurements was supported by the RFBR-JSPS Grant No. 18-52-50022 and RFBR Grant No. 18-32-20058. The calculations were conducted using the equipment of the Shared Resource Center “Far Eastern Computing Resource” IACP FEB RAS (see Ref. [59]).

-
- [1] D. J. Thouless, *Phys. Rev. Lett.* **39**, 1167 (1977).
 [2] D. Thouless, *Phys. Rep.* **67**, 5 (1980).
 [3] E. Abrahams, P. W. Anderson, D. C. Licciardello, and T. V. Ramakrishnan, *Phys. Rev. Lett.* **42**, 673 (1979).
 [4] B. L. Altshuler and A. G. Aronov, in *Electron-Electron Interactions in Disordered Systems*, edited by A. Efros and M. Pollak (North-Holland, Amsterdam, 1985).
 [5] G. Zala, B. N. Narozhny, and I. L. Aleiner, *Phys. Rev. B* **64**, 214204 (2001).
 [6] B. Narozhny, G. Zala, and I. Aleiner, *Physica E* **18**, 270 (2003).
 [7] I. G. Khalil, M. Teter, and N. W. Ashcroft, *Phys. Rev. B* **65**, 1953091 (2002).
 [8] Y. Weiss, M. Goldstein, and R. Berkovits, *Phys. Rev. B* **75**, 064209 (2007).
 [9] A. Yacoby, in *Strong Interaction in Low Dimensions*, edited by D. Baeriswyl and L. Degiorgi (Kluwer, Dordrecht, 2004), pp. 321–346.
 [10] S. Hikami, A. I. Larkin, and Y. Nagaoka, *Prog. Theor. Phys.* **63**, 707 (1980).
 [11] C. Brun, T. Cren, and D. Roditchev, *Supercond. Sci. Technol.* **30**, 013003 (2017).
 [12] T. Uchihashi, *Supercond. Sci. Technol.* **30**, 013002 (2017).
 [13] A. M. Gabovich, A. I. Voitenko, and M. Ausloos, *Phys. Rep.* **367**, 583 (2002).
 [14] Y. Yang, S. Fang, V. Fatemi, J. Ruhman, E. Navarro-Moratalla, K. Watanabe, T. Taniguchi, E. Kaxiras, and P. Jarillo-Herrero, *Phys. Rev. B* **98**, 035203 (2018).
 [15] M. Hoesch, L. Gannon, K. Shimada, B. J. Parrett, M. D. Watson, T. K. Kim, X. Zhu, and C. Petrovic, *Phys. Rev. Lett.* **122**, 017601 (2019).
 [16] X. Yang, Y. Zhou, M. Wang, H. Bai, X. Chen, C. An, Y. Zhou, Q. Chen, Y. Li, Z. Wang, J. Chen, C. Cao, Y. Li, Y. Zhou, Z. Yang, and Z. A. Xu, *Sci. Rep.* **8**, 1 (2018).
 [17] H.-H. Kim, S. M. Souliou, M. E. Barber, E. Lefrançois, M. Minola, M. Tortora, R. Heid, N. Nandi, R. A. Borzi, G. Garbarino, A. Bosak, J. Porras, T. Loew, M. König, P. J. W. Moll, A. P. Mackenzie, B. Keimer, C. W. Hicks, and M. Le Tacon, *Science* **362**, 1040 (2018).
 [18] M. Hücker, N. B. Christensen, A. T. Holmes, E. Blackburn, E. M. Forgan, R. Liang, D. A. Bonn, W. N. Hardy, O. Gutowski, M. V. Zimmermann, S. M. Hayden, and J. Chang, *Phys. Rev. B* **90**, 054514 (2014).
 [19] T. P. Croft, C. Lester, M. S. Senn, A. Bombardi, and S. M. Hayden, *Phys. Rev. B* **89**, 224513 (2014).
 [20] L. Li, X. Deng, Z. Wang, Y. Liu, M. Abeykoon, E. Dooryhee, A. Tomic, Y. Huang, J. B. Warren, E. S. Bozin, S. J. Billinge, Y. Sun, Y. Zhu, G. Kotliar, and C. Petrovic, *npj Quantum Materials* **2**, 1 (2017).
 [21] J. M. Tranquada, J. D. Axe, N. Ichikawa, A. R. Moodenbaugh, Y. Nakamura, and S. Uchida, *Phys. Rev. Lett.* **78**, 338 (1997).
 [22] J. A. W. Straquadine, F. Weber, S. Rosenkranz, A. H. Said, and I. R. Fisher, *Phys. Rev. B* **99**, 235138 (2019).
 [23] H. M. Jaeger, D. B. Haviland, B. G. Orr, and A. M. Goldman, *Phys. Rev. B* **40**, 182 (1989).
 [24] F. Couëdo, O. Crauste, A. A. Drillien, V. Humbert, L. Bergé, C. A. Marrache-Kikuchi, and L. Dumoulin, *Sci. Rep.* **6**, 6 (2016).
 [25] D. V. Gruznev, L. V. Bondarenko, A. Y. Tupchaya, V. G. Kotlyar, O. A. Utas, A. N. Mihalyuk, S. V. Eremeev, A. V. Zotov, and A. A. Saranin, *Phys. Rev. B* **98**, 125428 (2018).
 [26] A. A. Saranin, A. V. Zotov, V. G. Kotlyar, I. A. Kuyanov, T. V. Kasyanova, A. Nishida, M. Kishida, Y. Murata, H. Okado, M. Katayama, and K. Oura, *Phys. Rev. B* **71**, 035312 (2005).
 [27] G. Kresse and J. Hafner, *Phys. Rev. B* **47**, 558 (1993).
 [28] G. Kresse and D. Joubert, *Phys. Rev. B* **59**, 1758 (1999).
 [29] P. E. Blöchl, *Phys. Rev. B* **50**, 17953 (1994).
 [30] J. P. Perdew and A. Zunger, *Phys. Rev. B* **23**, 5048 (1981).
 [31] L. G. Ferreira, M. Marques, and L. K. Teles, *Phys. Rev. B* **78**, 125116 (2008).
 [32] L. G. Ferreira, M. Marques, and L. K. Teles, *AIP Adv.* **1**, 032119 (2011).
 [33] J. E. Hoffman, K. McElroy, D.-H. Lee, K. M. Lang, H. Eisaki, S. Uchida, and J. C. Davis, *Science* **297**, 1148 (2002).
 [34] L. Chen, P. Cheng, and K. Wu, *J. Phys.: Condens. Matter* **29**, 103001 (2017).
 [35] R. E. Thorne, *Phys. Today* **49**(5), 42 (1996).
 [36] C. Brun, Z.-Z. Wang, and P. Monceau, *Phys. Rev. B* **80**, 045423 (2009).
 [37] C. Brun, S. Brazovskii, Z.-Z. Wang, and P. Monceau, *Physica B* **460**, 88 (2015).
 [38] Y. Nakata, K. Sugawara, S. Ichinokura, Y. Okada, T. Hitosugi, T. Koretsume, K. Ueno, S. Hasegawa, T. Takahashi, and T. Sato, *Npj 2D Mater. Appl.* **2**, 12 (2018).
 [39] K. W. Clark, X.-G. Zhang, G. Gu, J. Park, G. He, R. M. Feenstra, and A.-P. Li, *Phys. Rev. X* **4**, 011021 (2014).
 [40] M. Z. Hossain, Y. Yamashita, K. Mukai, and J. Yoshinobu, *Phys. Rev. B* **67**, 153307 (2003).
 [41] G. W. Brown, H. Grube, M. E. Hawley, S. R. Schofield, N. J. Curson, M. Y. Simmons, and R. G. Clark, *J. Vac. Sci. Technol. A* **21**, 1506 (2003).

- [42] A. F. Ioffe and A. R. Regel, in *Progress in Semiconductors*, edited by A. F. Gibson, F. A. Kroger, and R. E. Burgess (Heywood, London, 1960), Vol. 4, pp. 237–291.
- [43] M. Graham, C. Adkins, H. Behar, and R. Rosenbaum, *J. Phys.: Condens. Matter* **10**, 809 (1998).
- [44] See Supplemental Material at <http://link.aps.org/supplemental/10.1103/PhysRevB.100.155412> for details on (1) effect of defect density on sample metallicity and (2) fitting of temperature dependence of sheet resistance to the AL-MT corrections.
- [45] M. Pollak, *J. Non-Cryst. Solids* **11**, 1 (1972).
- [46] E. M. Hamilton, *Philos. Mag.* **26**, 1043 (1972).
- [47] N. F. Mott, *J. Non-Cryst. Solids* **1**, 1 (1968).
- [48] A. L. Efros and B. I. Shklovskii, *J. Phys. C* **8**, L49 (1975).
- [49] P. Dai, Y. Zhang, and M. P. Sarachik, *Phys. Rev. Lett.* **69**, 1804 (1992).
- [50] L. Aslamazov and A. Larkin, *Sov. Phys. Solid State* **10**, 875 (1968).
- [51] F. Sharifi, A. V. Herzog, and R. C. Dynes, *Phys. Rev. Lett.* **71**, 428 (1993).
- [52] A. Larkin and A. Varlamov, *Theory of Fluctuations in Superconductors*, International Series of Monographs on Physics (Oxford University Press, New York, 2005).
- [53] K. Maki, *Prog. Theor. Phys.* **39**, 897 (1968).
- [54] R. S. Thompson, *Phys. Rev. B* **1**, 327 (1970).
- [55] H. R. Khan, *Gold Bull.* **17**, 94 (1984).
- [56] Y. Wu, M. C. Duan, N. Liu, G. Yao, D. Guan, S. Wang, Y. Y. Li, H. Zheng, C. Liu, and J. F. Jia, *Phys. Rev. B* **99**, 140506(R) (2019).
- [57] S.-K. Yip, *Phys. Rev. B* **41**, 2612 (1990).
- [58] P. Carretta, D. V. Livanov, A. Rigamonti, and A. A. Varlamov, *Phys. Rev. B* **54**, 9682(R) (1996).
- [59] <https://cc.dvo.ru>